Supplementary Information for

Electroreduction of Carbon Dioxide (CO_2) at Oxalate and Polypyrrole Modified Copper Surfaces

Minyoung Kim,[a] Meredith Zannacker,[b] Yuxuan Zhang,[a] Reilly Eiynck,[b] Reese Resheske,[b] Donghun Lee,[a] Ella Mack,[b] Elijah Behnke,[b] Sunghwan Lee[a*] and Sujat Sen[b*]

[a]School of Engineering Technology, Purdue University, West Lafayette, IN, 47907, USA

[b]Department of Chemistry & Biochemistry, University of Wisconsin-Lacrosse, Lacrosse, WI, 54601, USA

E-mail: ssen@uwlax.edu and sunghlee@purdue.edu

This file includes:

S.1. Preparation of gas diffusion electrodes

PTFE-based TE35 filter discs with 0.2 μm pore size, 47 mm diameters, and a polypropylene (PP) support ring on one side (Whatman, Sigma Aldrich) were used as the GDL, hereon referred to as "TE35" substrates. The TE35 substrates were modified with catalyst and used as the foundation for all GDEs in this study and optical images of the same are shown in Fig. S1. Nominal thickness of these substrates was determined to be 254 ± 5 μm, (Mitutoyo Model#7326A) as purchased from the manufacturer. The Teflon side of the GDL was coated with catalyst particles by thermal evaporation. Copper (Cu) thin films were evaporated onto glass, Si, and Teflon/GDL substrates to a thickness ranging 100-1000 nm at a working pressure of 2×10^{-3} Torr. Prior to the depositions, the evaporator chamber was pumped down to a base pressure of ~5×10^{-6} Torr or below. The thickness of the films was monitored in-situ through quartz crystal microbalance with a gold-coated crystal and validated ex-situ using an FS-1 multiwavelength ellipsometer (FilmSense). The sheet resistance of deposited Cu films was measured using a custom-built four-point probe with a precision multimeter (Keithley 2000).

S.2. Electrochemical cell Design & Electrolysis experiments

The flow fields, which also serve as current collectors, were machined from 3.18 mm thick impregnated graphite (G347B, MWI, Inc.) with 12 mm × 1 mm rectangular slots for inlet and outlet gas flow such that all the reactants are forced through the porous electrode in a flow-through configuration. The GDEs were sealed into the cell using gaskets cut from 1/16 in. thick, 60A durometer hardness, butyl rubber sheets (McMaster-Carr). The entire cell was assembled and tightened using a torque screwdriver (Mountz Inc.) with a torque of 14 – 16 lb_f-in (1.6 – 1.8 N-m). To ensure accuracy, before every experiment, the potential of the Ag/AgCl reference

electrode was measured against a saturated calomel electrode (Fisher Scientific, nominally +242 mV vs. SHE) dedicated for calibration and not for experiments that could compromise its integrity. The difference in potential was always within ± 20 mV of the expected value. The exact value within that 20 mV range was not recorded and contributes to the experimental uncertainty in all reported electrode potentials. For comparison with other reporting scales, the Ag/AgCl electrode potentials can be converted to the reversible hydrogen electrode (RHE) scale, within ± 20 mV accuracy, via the following equation: E (RHE) = E (Ag/AgCl) + 0.210 + 0.0591 × pH. In this study, the electrolyte used was 1M $KHCO_3$ (99.999%, Sigma Aldrich, Trace Metal impurities < 10 ppm) dissolved in deionized water (Type 1, filtered to 18.2 MΩ.cm using Gen Pure Water purifier, ThermoScientific). Saturated with CO_2, this electrolyte had a pH of 7.6 and this is assumed to be constant through the course of the electrolysis. Reported potentials can be inter-converted between the SHE, Ag/AgCl or RHE scales based on this conversion.

During electrolysis operation, CO_2 (99.99%, Research Grade 5.0, Mississippi Welders Supply Company, MWSCO) was delivered to the cathode at a constant flow rate of 20 mL min-1 using mass flow controllers (Alicat Scientific). The CO_2 stream were supplied to the MFCs directly from the tank without any hydration. An aqueous electrolyte solution of 1M $KHCO_3$ (99.999%, Sigma Aldrich, Trace Metal impurities < 10 ppm) dissolved in deionized water (Type 1, filtered to 18.2 MΩ.cm using Gen Pure Water purifier, ThermoScientific) was used as both catholyte and anolyte and pre-saturated with a secondary stream of 20 ccm CO_2 before it was passed through the cell using a peristaltic pump (Masterflex L/S Series) at a constant volumetric flow rate of 1 mL min^{-1}. On the catholyte stream, a single pass configuration was used to minimize product crossover and loss due to oxidation at the anode. The anolyte stream was recirculated for the duration of the experiment. Silicone tubing (Masterflex, L/S 14) was used inside the pump head,

while perfluoroalkoxy alkane (PFA) tubing (Swagelok) connected the pump head, reservoir, and flow cell together. All tubing connections were coupled together with PFA or stainless-steel compression fittings (Swagelok). Experiments were performed at room temperature with no temperature measurement and controls were not included within the cell. Gaseous products in the effluent gas stream were collected from two sources, which included the CO_2 stream existing the cathodic half-cell as well as the secondary CO_2 stream existing the catholyte reservoir. These gas streams were injected one at a time via a 6-way valve (Swagelok, SS-43Y6FS2) into the automated sample loop of a gas chromatograph (GC, SRI Instruments MG#4). Before each electrolysis run, the sample was treated to a pre-reduction by application of –5 mA/cm^2 for 1 hour to ensure the conversion of any oxidized species to metallic copper. The electrolyte samples generated during the pre-reduction step were analyzed and were not found to contain any appreciable products. Regardless, to ensure no contamination and eliminate the possibility of the oxalate contributing to eCO_2RR, a fresh electrolyte was introduced thereafter for each test.

S.3. Experimental details of oxalate and polypyrrole deposition

For copper oxalate deposition, a typical deposition bath of 25 mL consisted of 0.3M oxalic acid in Type-1 deionized (DI, Resistivity ~18.2 MOhm.cm) water circulating through the cell at 1 mL/min using a peristaltic pump. Preliminary tests conducted without flowing electrolyte revealed heterogeneous and patchy depositions suggesting localized effects, which were largely absent after flow was introduced. Additionally, the presence of O_2 (from air) was found necessary for the deposition of a uniform oxalate film, and initial trials conducted with continuous N_2 purging failed to produce stable films. A pristine Cu-coated TE35 substrate was used as the working electrode, a Platinum sheet was the counter electrode and a freshly

calibrated Ag/AgCl (+0.210 V vs. SCE) was used as the reference electrode. All electrochemical experiments were conducted using a VSP-300 Multichannel potentiostat (Bio-logic) in a three-electrode configuration. Cyclic voltammetry between -0.3V to +0.4V vs. Ag/AgCl[1] was used to generate thin films of copper oxalate on the surface of the thermally evaporated metallic copper and variations were explored with respect to both number of cycles and scan rate.

Electrodeposition of pyrrole was conducted in the same single compartment flow cell, immediately following the oxalate deposition. A typical deposition bath for pPy deposition consisted of 0.3M oxalic acid and 0.1M freshly distilled pyrrole (colorless) dissolved in DI water. Deposition was conducted using a constant applied potential of 0.9V vs. Ag/AgCl for varying durations of time to obtain a target charge (coulombs passed) which ranged from a thin sample (0.25C), medium thickness (2C), and very thick deposition (10C).

S.4. Characterization of polypyrrole on copper-based GDL

Using the oxalate modified films, pPy was successfully grown by applying a constant potential above 0.7 V (vs. Ag/AgCl) which was found to be a minimum threshold for the oxidative polymerization of pyrrole, consistent with prior literature reports.[1] The passivated copper oxalate coated Cu/TE35 substrates (3 cycles) were used as the working electrode and electropolymerization of the monomer was conducted in the same electrolyte used for the oxalate deposition. pPy films were successfully grown at a constant applied voltage of 0.9V (vs. Ag/AgCl) in this study and a sample chronoamperogram is shown in Fig. S9. The charge passed during the deposition was used to control the approximate thickness of the pPy layer on top of the copper oxalate sub-layer. Fig. 2(d) shows a photograph which indicates complete and uniform coverage of the sample with a black-color pPy film such that the underlying copper or

copper oxalate are no longer visible. Fig. 2 also displays magnified SEM images, showing more densely compacted spherical structures compared to that of oxalate-coated counterparts, again consistent with prior literature reports.[1,2]

The structural integrity of the underlying catalyst after polymer deposition was further verified via XRD analysis (Fig. 2(m)). The diffraction pattern of the CuOA3_pPy2 sample retains the distinct peaks corresponding to copper oxalate (CuC_2O_4) and metallic copper, with slightly reduced peak intensity, suggesting that electropolymerization process did not induce significant phase decomposition of the underlying copper and copper oxalate layer, even though a portion of the copper oxalate phase might have been partially consumed or lost its crystallinity. This confirms that the electropolymerization process did not induce any phase decomposition or structural degradation of the underlying copper and copper oxalate layer. To further confirm the successful deposition of pPy and the preservation of the layers beneath, cross-sectional FIB-SEM and FTIR analyses were conducted. FIB-SEM images (Fig. S7) clearly revealed a distinct three-layered structure consisting of evaporated Cu, copper oxalate, and the pPy overlayer. Furthermore, FTIR spectra (Fig. S8) confirmed the coexistence of vibrational peaks characteristic of both copper oxalate and polymerized pPy, verifying that the oxalate layer was structurally preserved beneath the polymer coating.

In Fig. S17, the as-prepared CuOA3_pPy0.25 shows predominantly positively charged nitrogen's, the sum of $C–N^+$ and $C=N^+$ occupying 62.65% of the total area, consistent with p-doped pPy. After the electrolysis, the summed fraction of polaron and bipolaron drops to 19.66%, while the neutral pyrrolic NH-Py at 399.84 eV increased to 48.18% from 37.35% in as-prepared sample and a new component at 398.29 eV (32.16%) emerged, assignable to

imine-like/pyridinic nitrogen (C=N) and possibly interfacial Cu–N coordination (Fig. S19a). The decrease in positively charged nitrogen indicates reduction and de-doping of charged pPy under reducing eCO_2RR environment. Upon slight surface etching of the post-electrolysis film, the C=N signal decreases to 23.79% and the NH-Py peak increases to 54.08%, indicating a depth-graded doping profile from the electrolyte-polymer interface toward polymer-catalyst interface. The outermost layer is imine-enriched owing to cathodic de-doping and counter-anion expulsion, often accompanied by densification to a less-porous morphology,[3,4] potentially reinforced by local OH^- accumulation during the eCO_2RR.[5,6] In contrast, the subsurface retains a higher fraction of doped N centers, thereby maintaining its electrical conductivity. Such a barrier surface–conductive sublayer architecture can secure electronic transport to the underlying Cu-based catalysts while limiting ion permeation through the denser, less conductive outer skin.[7]

S.5. Density Functional Theory (DFT) studies

First-principles calculations were carried out using density functional theory (DFT) as implemented in the Vienna Ab initio Simulation Package (VASP). The generalized gradient approximation (GGA) with the Perdew–Burke–Ernzerhof (PBE) functional was employed to describe the exchange–correlation interactions. To better account for weak van der Waals interactions, the D3 dispersion correction with the Grimme scheme was applied. An energy cutoff of 600 eV and a Monkhorst-Pack k-mesh of 2 × 2 × 1 were employed to sample the Brillouin zones of the crystals, both with and without the adsorption. The adsorption energy (E_{ads}) was calculated from the energy differences between the adsorbent on the substrate surface (E_{total}) and the sum of the energy of the substrate crystal (E_{sub}) and the total energy of the adsorbate ($E_{adsorbate}$), defined as $E_{ads} = E_{total} – (E_{sub} + E_{adsorbate})$. A vacuum layer of approximately 15 Å was

applied to prevent interactions between adjacent slabs. For all calculations, the criterion for the electronic self-consistent field loop was set to 1×10^{-5} eV per atom. Atomic structures were optimized until the residual forces were below 0.05 eV $Å^{-1}$. We focused on distinguishing our (a) CuOA 3 oxalate-derived catalyst which has ~77% Cu^+ per XPS data from (b) cuprite surface (Cu_2O) which is by definition 100% Cu^+. Since Cu^+ was the dominant species for both these systems, and they share the same underlying crystal structure, the Cu:O stoichiometry of the two models was adjusted according to the XPS results (Table S4). In order to create the oxalate-derived surface, we used the pristine cuprite Cu_2O model and modified its local coordination and electronic environment by using the experimentally determined ratio between Cu^0 and Cu^+ species. This treatment enables the two structures to be distinguished in terms of their surface electronic structure and local coordination characteristics.

For the adsorption configuration, the atop adsorption geometry was adopted as the initial model, which is commonly observed for carbonyl-containing intermediates on metal oxide surfaces due to its favorable orbital interaction with surface Cu sites. The adsorption energy was calculated using the following expression:

$$E_{ads} = E_{total} - (E_{sub} + E_{adsorbate})$$

where E_{total}, E_{sub}, and $E_{adsorbate}$ represent the total energies of the adsorbate–surface complex, the clean surface, and the isolated adsorbate, respectively. Furthermore, the optimized adsorption configurations of related reaction intermediates, including CH_3CO*, CH_3CHO*, CH_3CH_2O*, and CH_3COCHO*, on both cuprite Cu_2O and oxalate-derived surfaces were studied as shown in Fig. S20. These were subsequently used for the reaction energy barrier analysis as described below.

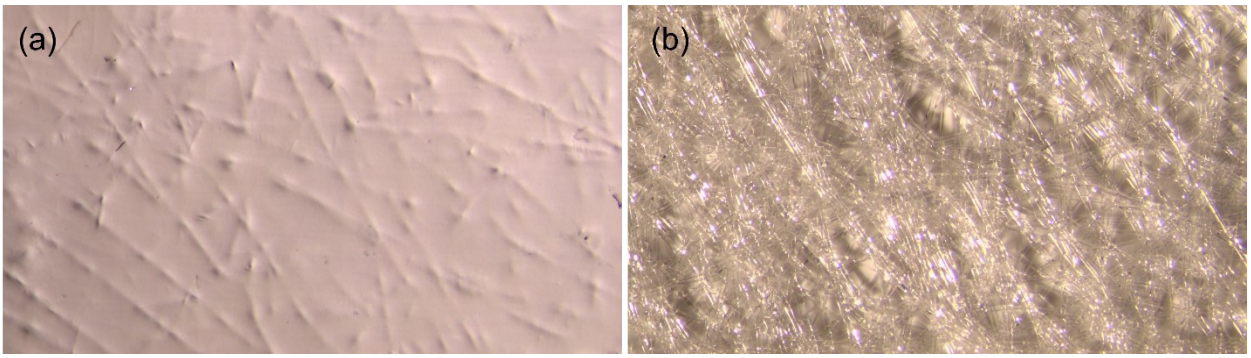

Figure S1. *Photographs of (a) front side of the TE35 substrate as purchased, and (b) back side of the TE35 substrate as purchased.*

Figure S1. shows optical images of the commercially available TE35 substrate used in this study. Optical inspection of this pristine substrate reveals a fabric-like inter-woven fiber matrix structure on one side (polypropylene support ring as per manufacturer) and the other side to be a relatively smoother Teflon film with no visible structure. This mimics the bilayer structure of conventional substrates such as the carbon-based gas diffusion layers (GDL) used in fuel cells.

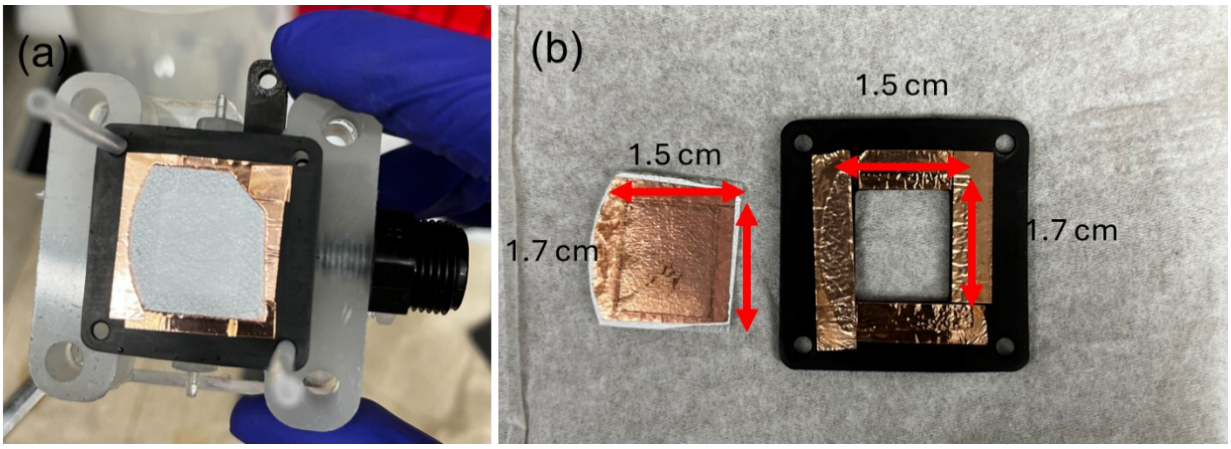

Figure S2. *Photographs demonstrating how copper tape was used to make electrical contact with the front of the catalyst surface and current collector placed on the back.*

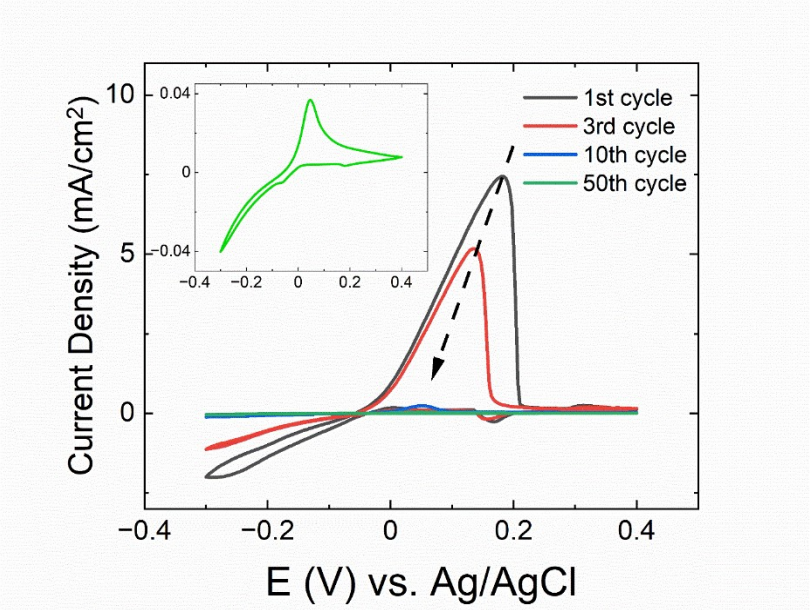

Figure S3. *Cyclic voltammogram of Cu/TE35 at 1 mV/s between -0.3V and +0.4V vs. Ag/AgCl for a total of 50 cycles. Electrolytes used was 0.3M aqueous oxalic acid solution flowing constantly at 1 mL/min; inset shows the last cycle in more detail.*

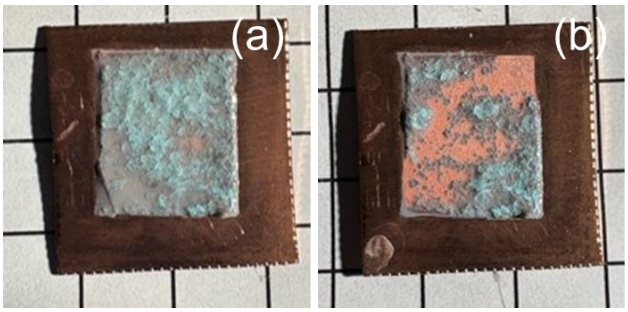

Figure S4. *Photographs of oxalate deposition on commercially available planar copper substrates (McMaster Carr) (a) immediately after deposition and (b) after gently rinsing with a stream of DI water. Deposits were found to be non-uniform and weakly adherent which came off during post-deposition rinsing.*

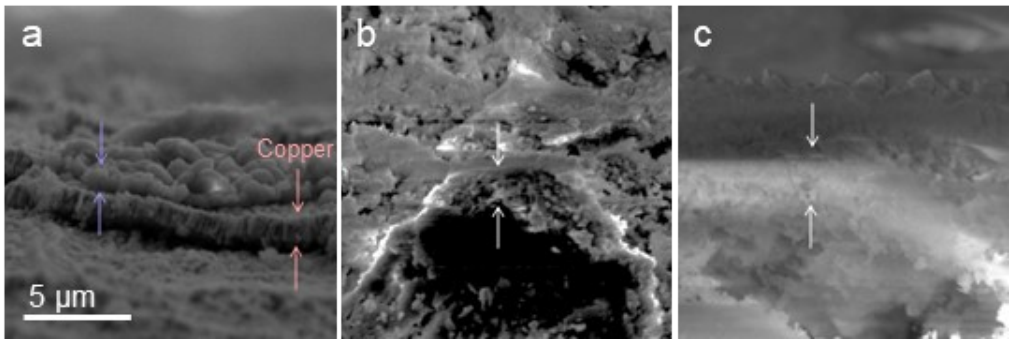

Figure S5. *Cross-sectional SEM images of (a) CuOA 3, (b) CuOA 10, and (c) CuOA 50.*

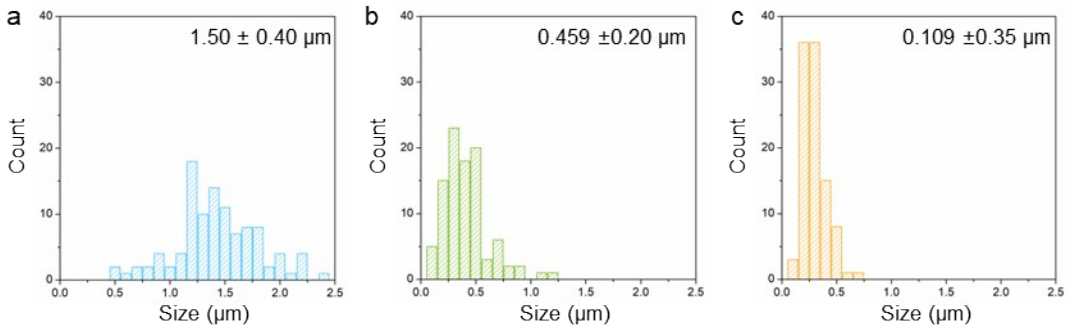

Figure S6. *Particle size distribution histograms obtained from top-view SEM images of (a) CuOA 3, (b) CuOA 10, and (c) CuOA 50.*

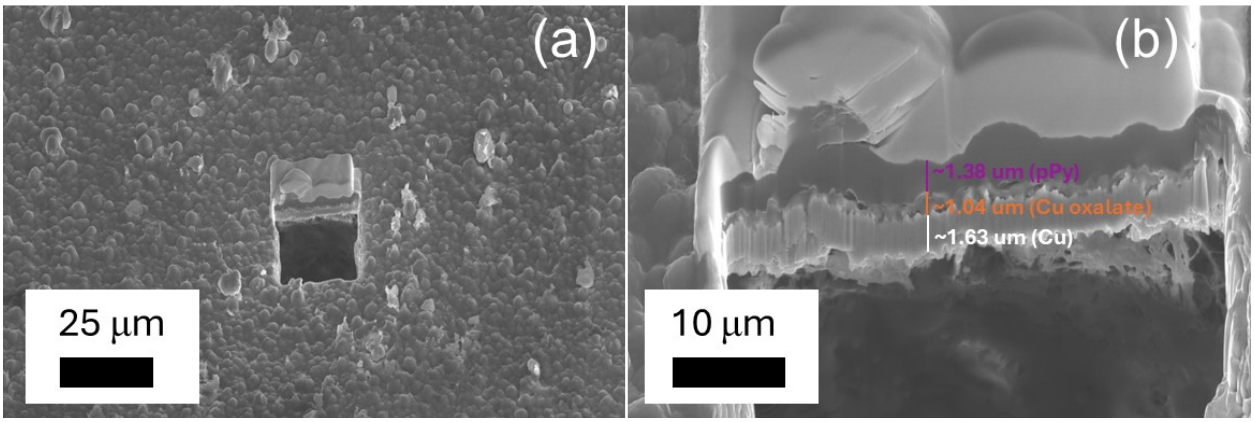

Figure S7. *FIB-SEM image of CuOA3_pPy2 sample that exhibits distinct layers of the Teflon substrate, copper metal layer, copper oxalate layer and polypyrrole coating on top. The Etching was capped by a protective Platinum layer deposited to minimize beam damage. The FIB-cut edge exhibited distinct three-layered structure with clear interfaces, consisting of evaporated Cu (1.63 µm), copper oxalate (1.04 µm), and pPy layer (1.38 µm).*

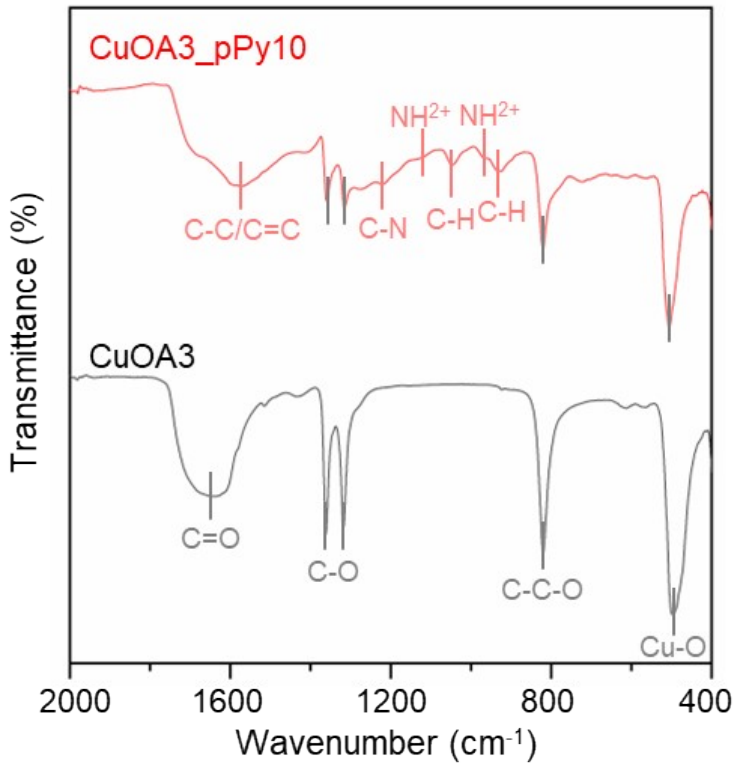

Figure S8. *FTIR spectra of CuOA 3 and CuOA3_pPy10 exhibiting unique bond stretches that identify the presence of oxalate and polypyrrole respectively.*

Data was collected using an ATR accessory on a Thermo Nicolet S50 instrument and bond stretches marked were identified on the basis of prior literature. [8–12] *The CuOA3 exhibited clear peaks representing Cu-O (493 cm^{-1}), C-C-O (821 cm^{-1}), C-O (1318 and 1361 cm^{-1}), and C=O (1647 cm^{-1}) stretching/bending, which are typical for copper oxalate species. After pPy deposition, the spectrum displayed a coexistence of both copper oxalate (grey marks) and pPy (red marks) peaks. The new pPy-related peaks include C-H out-of-plane deformation (493 cm^{-1}), NH^{2+} (965 and 1127 cm^{-1}), C-H in-plane deformation (1047 cm^{-1}), C-N stretching (1217 cm^{-1}), and C-C/C=C stretching (1567 cm^{-1}), which are characteristic hallmarks for polymerized pPy, distinct from the pyrrole monomer.*

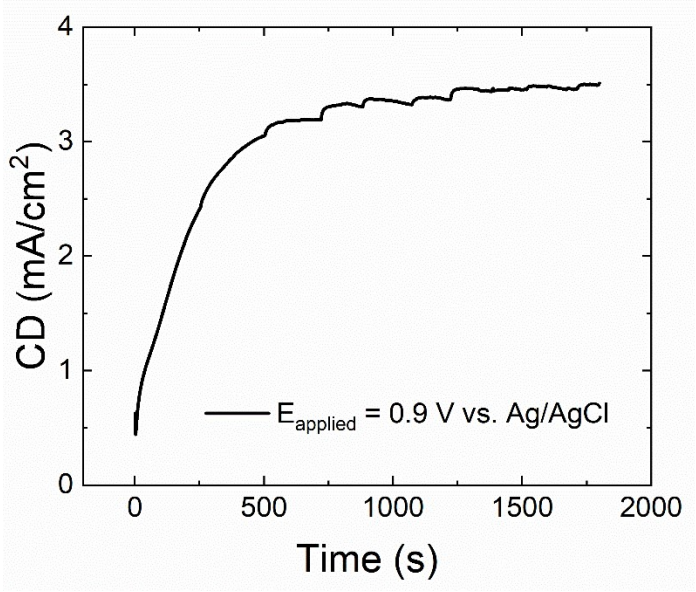

Figure S9. *Chronoamperogram recorded during a typical experiment where polypyrrole was grown on the surface of a CuOA 3 surface at a constant potential held for varying duration to adjust the total charge passed.*

Figure S9 shows a typical chronoamperogram where the current steadily rises and stabilizes over 30 minutes indicating the growth of a conductive polymer film on top of the copper oxalate coated substrate. Charge passed during the deposition at a typical deposition potential of 0.9V (vs. Ag/AgCl) was used to control the approximate thickness of the pPy layer on top of the copper oxalate sub-layer.

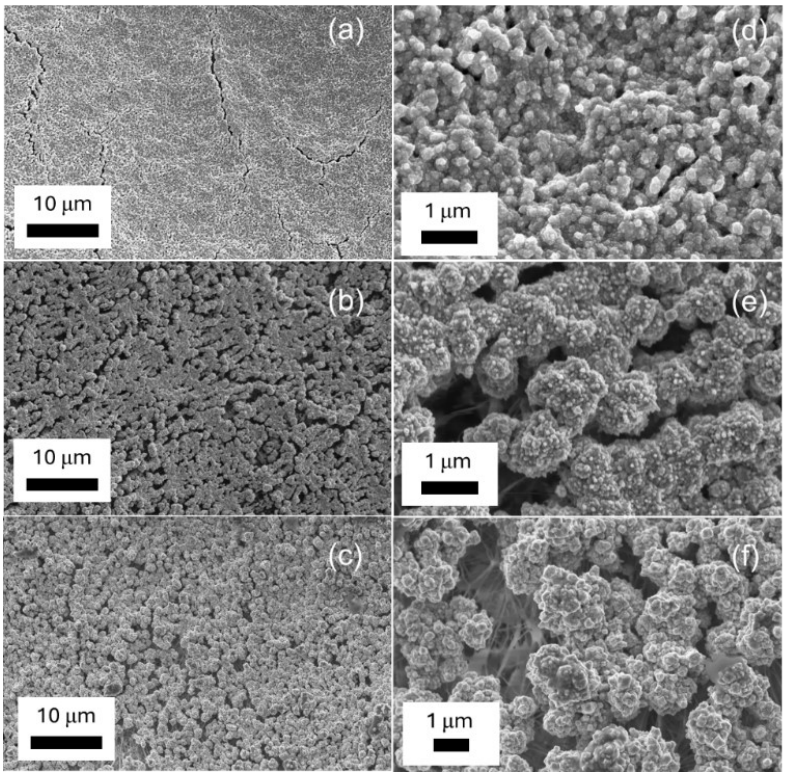

Figure S10. *SEM images of copper oxalate modified electrodes, CuOA 3 (a, d), CuOA 10 (b, e) and CuOA 50 (c, f) after pre-reduction treatment at low (left column) and high (right) magnification.*

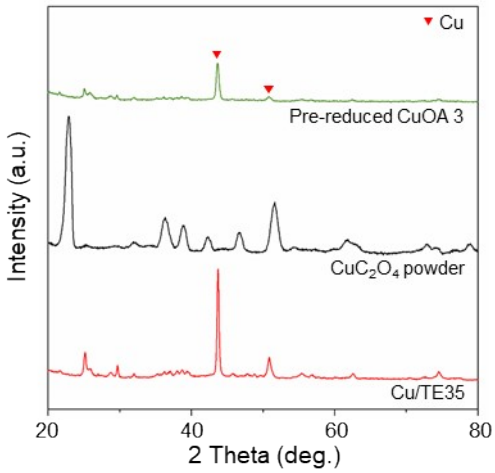

Figure S11. *XRD patterns of pre-reduced CuOA 3 (oxalate-derived surface), reference CuC_2O_4 powder, and Cu/TE35 samples with characteristic Cu (PDF 04-009-2090) and CuC_2O_4 (PDF 04-021-4364) peaks indicated.*

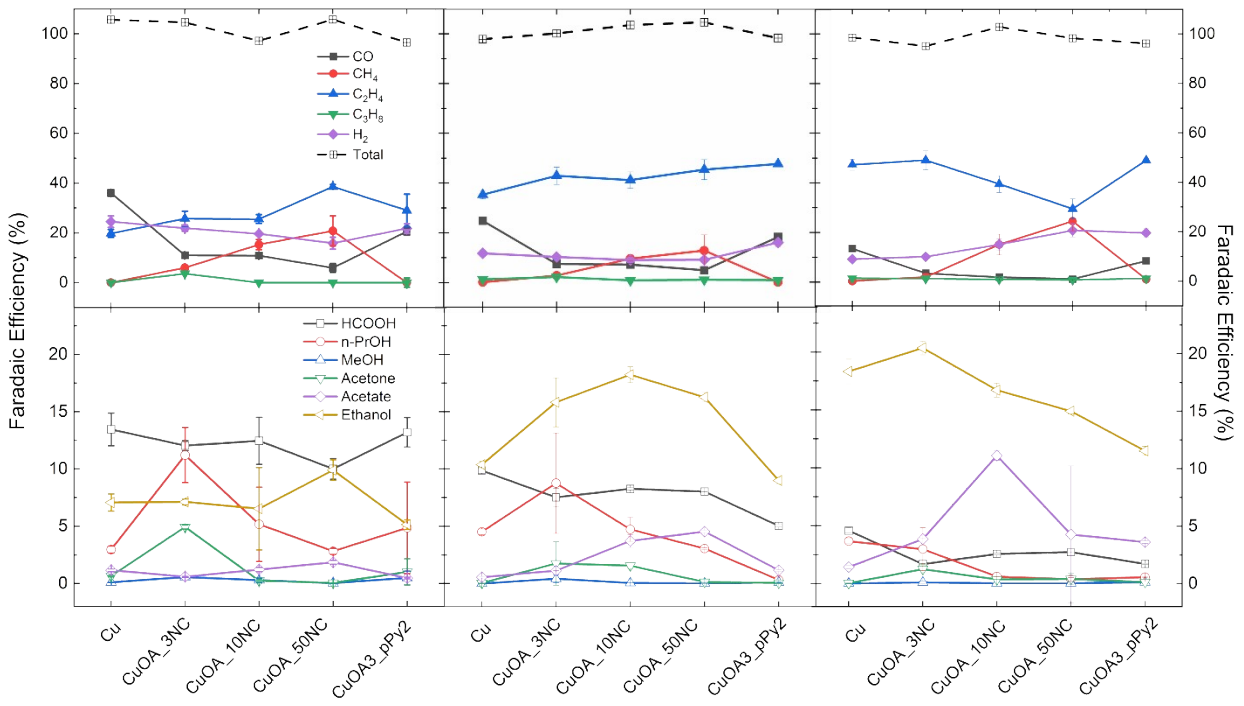

Figure S12. *Plot of faradaic efficiency for all products generated during galvanostatic CO_2 electrolysis at pristine copper, oxalate-coated copper and polypyrrole coated copper at various current densities. Top row shows all gaseous products, while bottom row shows all liquid phase products.*

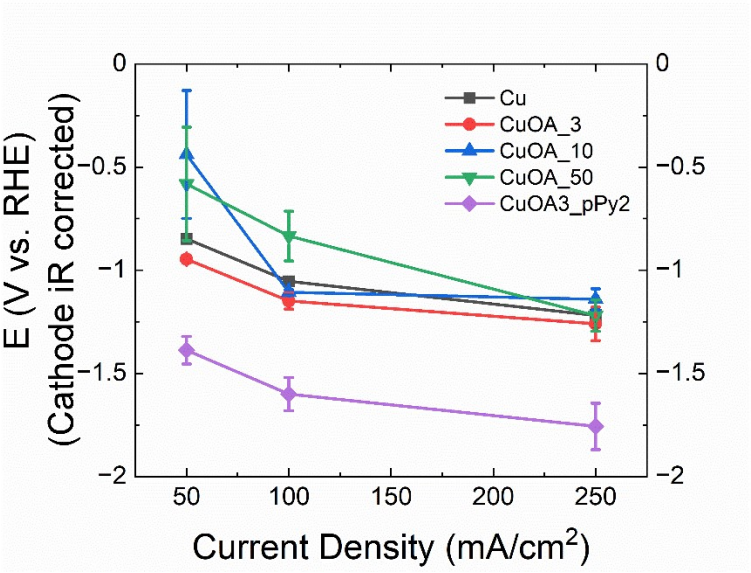

Figure S13. *Plot of cathode potential (iR corrected vs. RHE) as a function of applied current density during galvanostatic reduction of* CO_2.

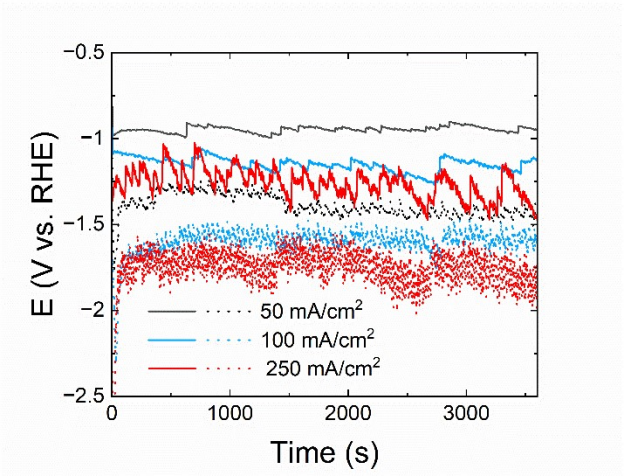

Figure S14. *Plot of cathode potential (iR corrected vs. RHE) as a function of time over the course of a 1hr electrolysis at CuOA 3 (solid lines) and CuOA3_pPy2 (dotted lines)*

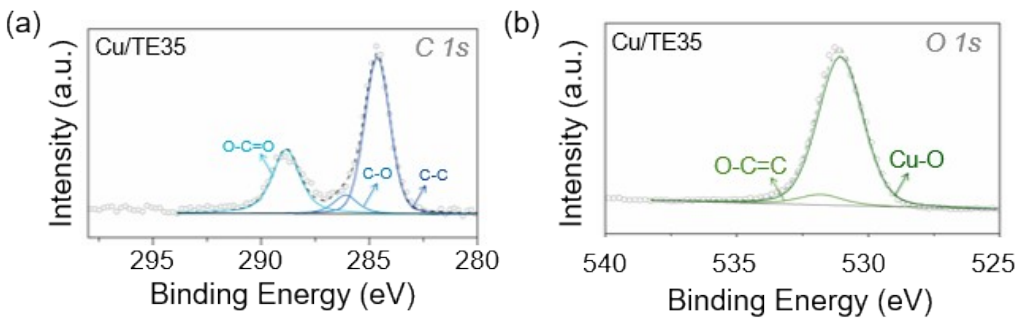

Figure S15. *High-resolution XPS spectrum of Cu/TE35 GDL in (a) C 1s and (b) O 1s region.*

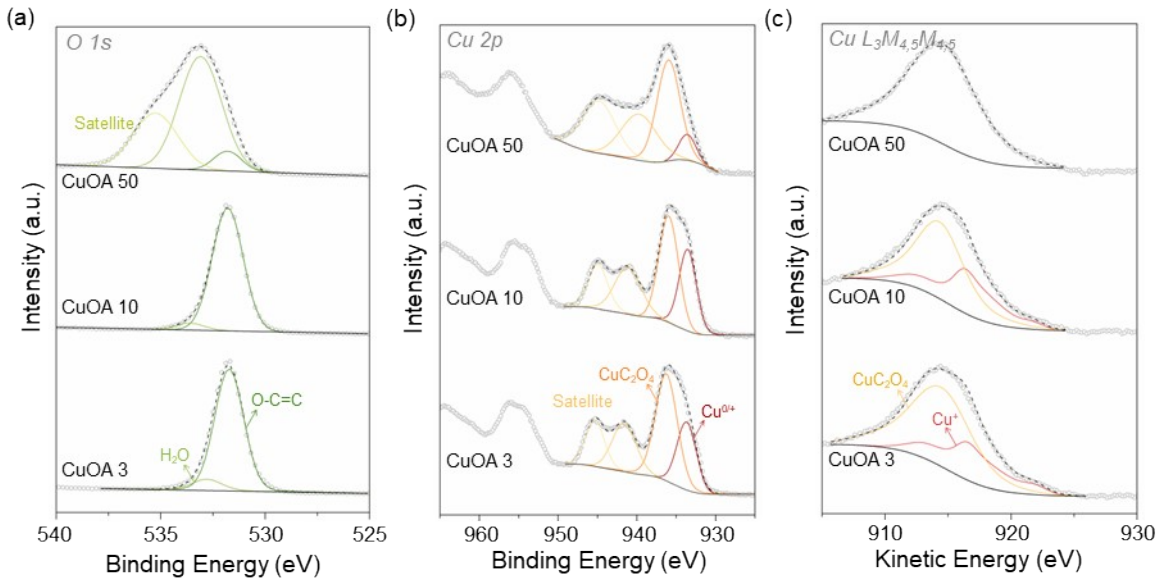

Figure S16. *High-resolution XPS spectrum of CuOA 3, 10, and 50 samples in (a) O 1s, (b) Cu 2p, and (c) Cu $L_3M_{4,5}M_{4,5}$ region.*

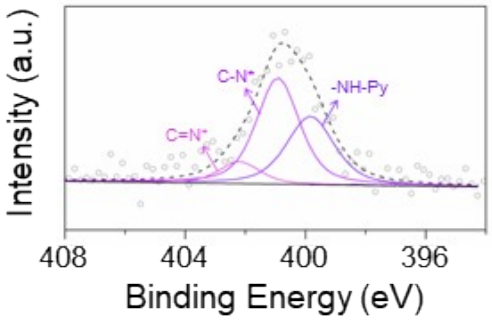

Figure S17. *High-resolution XPS spectrum of pristine CuOA3_pPy0.25 in N 1s region.*

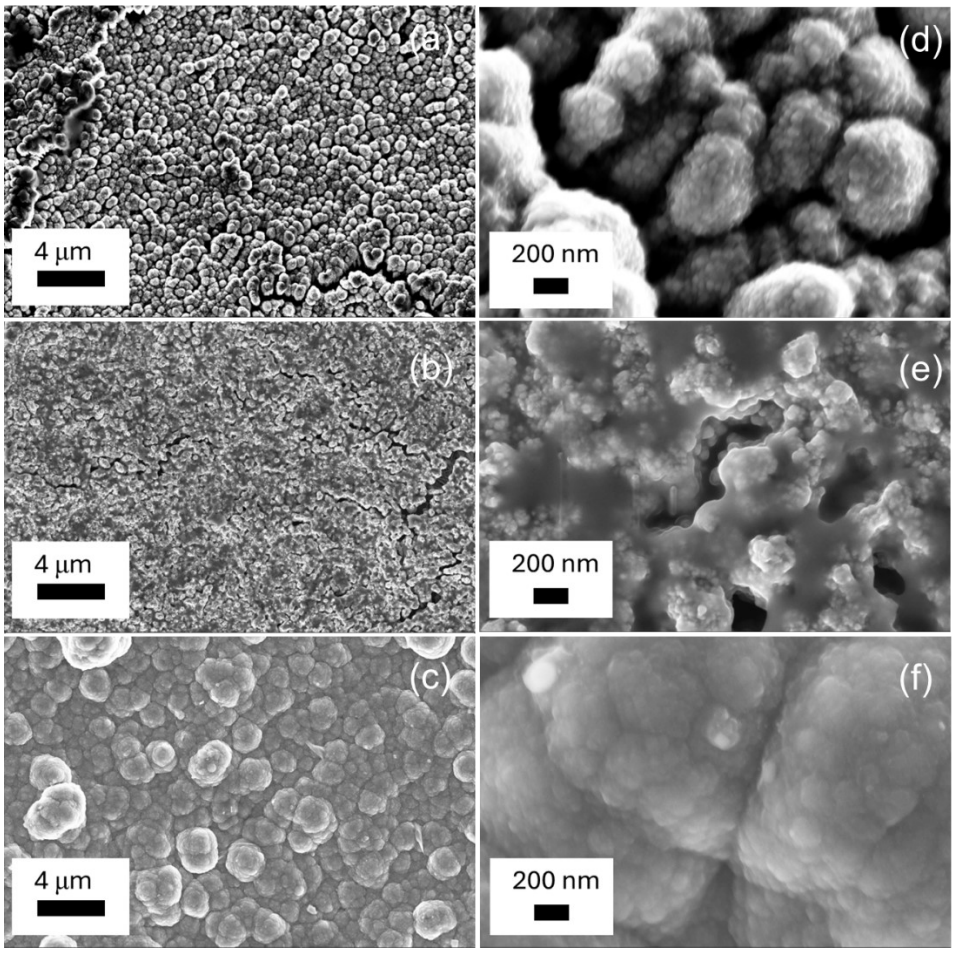

Figure S18. *SEM images of various cathodes after electrolysis testing, Cu/TE35 (a.d), CuOA 3 (b, e) and CuOA3_pPy2 (c, f) at low (left column) and high (right) magnification.*

Small amount of salt deposits were also seen on these electrodes which are likely due to residual electrolyte ($KHCO_3$) used during electrolysis that remains even after rinsing with DI water. Interestingly the polymer coated CuOA3_pPy2 electrode showed minimal change with a unform coverage of the polymer visible at both low and high magnifications suggesting that the polymer coating is robust, and imparts stability to the composite cathode, which could extend the usable lifetime of the catalyst.

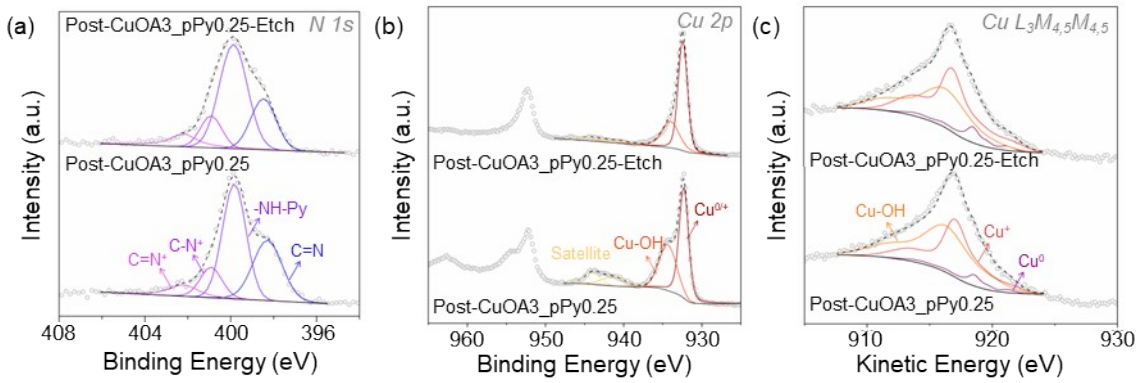

Figure S19. *High-resolution XPS in (a) N 1s, (b) Cu 2p region and (c) Cu $L_3M_{4,5}M_{4,5}$ Auger spectra of CuOA3_pPy0.25 and an etched CuOA3_pPy0.25 sample after eCO_2RR.*

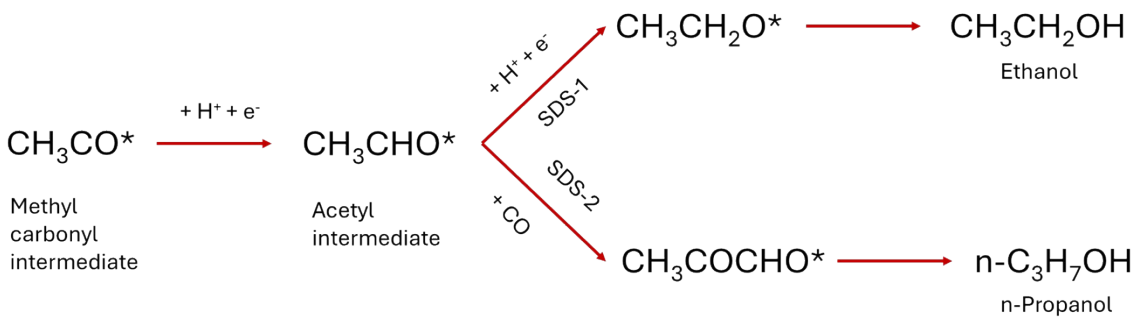

Figure S20. *Schematic of the reaction pathways starting from the methyl carbonyl intermediate leading to the selectivity determining steps which result in the formation of ethanol and n-propanol as products of eCO_2RR (Reproduced from[13])*

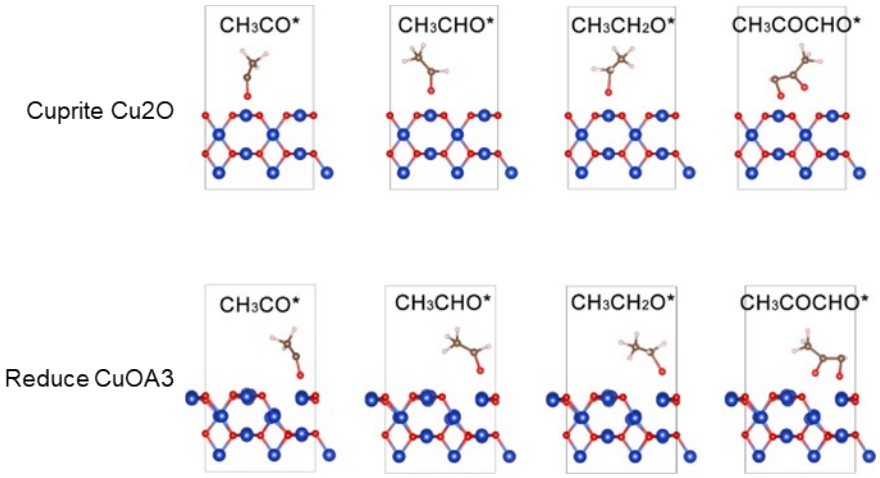

Figure S21. *Atomic models of reaction intermediates used for eCO_2RR energy barrier calculations on cuprite Cu_2O and reduced CuOA 3 oxalate-derived surface.*

Table S1. *Comparison of Cu-based catalysts reported in the literature for the eCO_2RR using a GDE-type flow cell configuration and near neutral pH electrolyte. C_{2+} products considered include ethylene, ethanol, ethane, acetate, and n-propanol.*

Catalyst	**Electrolyte**	**Maximum Geometric CD for C_{2+} (mA/cm^2)**	**Maximum Current Efficiency (CE) for C_{2+} (%)**	**Reference**
Cu/Copper Oxalate (CuOA3)	1M $KHCO_3$	195	79	This work
Cu/Copper Oxalate/pPy (CuOA3_pPy2)	1M $KHCO_3$	162	65	This work
Copper (II) Oxide Nanosheets	1M $KHCO_3$	410	~59	[14]
Reconstructed Copper	1M $KHCO_3$	347	77	[15]
Porous Copper	1M $KHCO_3$	91	~39	[16]
Cu cubes	1.2 M $KHCO_3$	183	61	[17]

Cu octahedra	1.2 M $KHCO_3$	63	32	[17]
Cu nanocrystals	Phosphate buffer (pH 6.4)	111	56	[18]
B-doped CuO	1M $KHCO_3$	55	62	[19]
Cu_2O hollow multi shell structures	0.5 M $KHCO_3$	514	77	[20]
FeTPP[Cl]/Cu	1M $KHCO_3$	250	82.6	[21]
Cu(100)-rich Cu hollow fiber	0.5 M $KHCO_3$	1444	62.8	[22]

Table S2. *Summary of XRD peak analysis for Cu (111), Cu (200), CuC_2O_4 (110), and CuC_2O_4 (120), including peak positions and crystalline sizes calculated by Scherrer's equation.*

	Cu (111)		Cu (200)	
	2 Theta	Size (nm)	2 Theta	Size (nm)
CuOA 50	-	-	-	
CuOA 10	-		-	
CuOA 3	43.36	22.60	50.48	13.54
Cu/TE35	43.33	18.55	50.45	11.70
	CuC_2O_4 (110)		CuC_2O_4 (120)	
	2 Theta	Size (nm)	2 Theta	Size (nm)
CuOA 50	23.21	33.28	36.45	18.28
CuOA 10	23.23	33.47	36.41	13.81
CuOA 3	22.92	23.82	36.52	10.23

Table S3. *Atomic composition of Cu/TE35, copper oxalate and polypyrrole on copper-based GDL from XPS survey analysis.*

	Cu	C	O	N	Cu:C:O
Cu/TE35	24.18	30.42	45.4		1:1.26:1.88
CuOA 3	13.46	35.83	50.71		1 : 2.66 : 3.77
CuOA 10	12.34	37.61	50.05		1 : 3.05 : 4.01
CuOA 50	10.11	42.83	47.06		1 : 4.24 : 4.65
CuOA3_pPy2	0	66.54	21.16	12.30	

Table S4. *Fitted area percentages of pristine Cu/TE35, copper oxalate and polypyrrole on copper-based GDL from high resolution XPS in Cu $2p_{3/2}$ and Cu LMM region.*

□	Cu 2p			Cu LMM			
□	CuC_2O_4	$Cu(OH)_2$	$Cu^{0/+}$	CuC_2O_4	$Cu(OH)_2$	Cu^{+}	Cu^{0}
Cu/TE35		48.33	51.67		40.43	40.54	19.03
CuOA 3	64.94		35.06	69.44		30.56	
CuOA 10	58.62		41.38	63.51		36.49	
CuOA 50	84.72		15.28	100			
CuOA3_pPy0.25	63.40		36.60	70.85		24.14	5.01
Pre-reduced CuOA 3		14.59	85.41		17.56	76.89	5.55

Table S5. *Fitted area percentages of post-electrolysis Cu/TE35, copper oxalate and polypyrrole on copper-based GDL from high resolution XPS in Cu $2p_{3/2}$ and Cu LMM region.*

	Cu 2p		Cu LMM		
	$Cu(OH)_2$	$Cu^{0/+}$	$Cu(OH)_2$	Cu^{+}	Cu^{0}
Cu/TE35	36.30	63.70	27.49	65.25	7.26
CuOA 3	67.30	32.70	68.01	29.56	2.44
CuOA3_pPy 0.25	40.14	59.86	51.58	42.26	6.16
CuOA3_pPy 0.25-Etch	31.76	68.24	42.04	49.48	8.48

References

1 P. Herrasti, A. I. del Rio and J. Recio, *Electrochimica Acta*, 2007, **52**, 6496–6501.

2 O. Devos, C. Gabrielli, L. Beitone, C. Mace, E. Ostermann and H. Perrot, *Journal of Electroanalytical Chemistry*, 2007, **606**, 85–94.

3 M. J. Higgins, S. T. McGovern and G. G. Wallace, *Langmuir*, 2009, **25**, 3627–3633.

4 S. Golba and J. Loskot, *Materials*, 2023, **16**, 7069.

5 G. G. McLeod, K. Jeffreys, J. M. R. MacAllister, J. Mundell, S. Affrossman and R. A. Petrick, *Journal of Physics and Chemistry of Solids*, 1987, **48**, 921–926.

6 A. J. Welch, A. Q. Fenwick, A. Böhme, H.-Y. Chen, I. Sullivan, X. Li, J. S. DuChene, C. Xiang and H. A. Atwater, *J. Phys. Chem. C*, 2021, **125**, 20896–20904.

7 X. Zhao, X. Liu, B. Fan and X. Zheng, *Polymers*, 2022, **14**, 1356.

8 H. Khojasteh, K. Heydaryan, P. Aspoukeh, H. N. Ibrahim, M. M. Mohammed, S. M. Sleman and M.-P. Mazhari, *Plasmonics*, 2025, **20**, 803–815.

9 A. Sunilkumar, S. Manjunatha, Y. T. Ravikiran, M. Revanasiddappa, M. Prashantkumar and T. Machappa, *Polym. Bull.*, 2022, **79**, 1391–1407.

10 A. Dianatdar, M. Miola, O. D. Luca, P. Rudolf, F. Picchioni and R. K. Bose, *J. Mater. Chem. C*, 2022, **10**, 557–570.

11 J. Stejskal, J. Vilčáková, M. Jurča, H. Fei, M. Trchová, Z. Kolská, J. Prokeš and I. Křivka, *Coatings*, 2022, **12**, 324.

12 H. Liu, G. Cui, L. Li, Z. Zhang, X. Lv and X. Wang, *Nanomaterials*, 2020, **10**, 166.

13 Y. Xue, X. Lv, C. Yang, L. Song, L. Zhang and G. Zheng, *Chem. Sci.*, 2025, **16**, 13944–13950.

14 X. Wang, K. Klingan, M. Klingenhof, T. Möller, J. Ferreira De Araújo, I. Martens, A. Bagger, S. Jiang, J. Rossmeisl, H. Dau and P. Strasser, *Nat Commun*, 2021, **12**, 794.

15 J. Lv, M. Jouny, W. Luc, W. Zhu, J. Zhu and F. Jiao, *Advanced Materials*, 2018, **30**, 1803111.

16 M. G. Kibria, C. Dinh, A. Seifitokaldani, P. De Luna, T. Burdyny, R. Quintero-Bermudez, M. B. Ross, O. S. Bushuyev, F. P. García De Arquer, P. Yang, D. Sinton and E. H. Sargent, *Advanced Materials*, 2018, **30**, 1804867.

17 G. L. De Gregorio, T. Burdyny, A. Loiudice, P. Iyengar, W. A. Smith and R. Buonsanti, *ACS Catal.*, 2020, **10**, 4854–4862.

18 H. S. Jeon, J. Timoshenko, C. Rettenmaier, A. Herzog, A. Yoon, S. W. Chee, S. Oener, U. Hejral, F. T. Haase and B. Roldan Cuenya, *J. Am. Chem. Soc.*, 2021, **143**, 7578–7587.

19 K. K. Patra, S. Park, H. Song, B. Kim, W. Kim and J. Oh, *ACS Appl. Energy Mater.*, 2020, **3**, 11343–11349.

20 C. Liu, M. Zhang, J. Li, W. Xue, T. Zheng, C. Xia and J. Zeng, *Angewandte Chemie International Edition*, 2022, **61**, e202113498.

21 F. Li, Y. C. Li, Z. Wang, J. Li, D.-H. Nam, Y. Lum, M. Luo, X. Wang, A. Ozden, S.-F. Hung, B. Chen, Y. Wang, J. Wicks, Y. Xu, Y. Li, C. M. Gabardo, C.-T. Dinh, Y. Wang, T.-T. Zhuang, D. Sinton and E. H. Sargent, *Nature Catalysis*, 2020, **3**, 75–82.

22 C. Zhu, Y. Song, X. Dong, G. Li, A. Chen, W. Chen, G. Wu, S. Li, W. Wei and Y. Sun, *Energy Environ. Sci.*, 2022, **15**, 5391–5404.